Nanoscale Advances

ROYAL SOCIETY OF CHEMISTRY

PAPER

View Article Online
View Journal | View Issue

Cite this: *Nanoscale Adv.*, 2022, **4**, 3353

Engineering thermoelectric and mechanical properties by nanoporosity in calcium cobaltate films from reactions of $Ca(OH)_2/Co_3O_4$ multilayers†

Binbin Xin, *[a] Erik Ekström, [a] Yueh-Ting Shih,[b] Liping Huang,[b] Jun Lu,[a] Anna Elsukova,[a] Yun Zhang,[c] Wenkai Zhu,[c] Theodorian Borca-Tasciuc, [c] Ganpati Ramanath,[ab] Arnaud Le Febvrier, [a] Biplab Paul [a] and Per Eklund *[a]

Controlling nanoporosity to favorably alter multiple properties in layered crystalline inorganic thin films is a challenge. Here, we demonstrate that the thermoelectric and mechanical properties of $Ca_3Co_4O_9$ films can be engineered through nanoporosity control by annealing multiple $Ca(OH)_2/Co_3O_4$ reactant bilayers with characteristic bilayer thicknesses (b_t). Our results show that doubling b_t, *e.g.*, from 12 to 26 nm, more than triples the average pore size from ~120 nm to ~400 nm and increases the pore fraction from 3% to 17.1%. The higher porosity film exhibits not only a 50% higher electrical conductivity of $\sigma \sim 90$ S cm^{-1} and a high Seebeck coefficient of $\alpha \sim 135$ μV K^{-1}, but also a thermal conductivity as low as $\kappa \sim 0.87$ W m^{-1} K^{-1}. The nanoporous $Ca_3Co_4O_9$ films exhibit greater mechanical compliance and resilience to bending than the bulk. These results indicate that annealing reactant multilayers with controlled thicknesses is an attractive way to engineer nanoporosity and realize mechanically flexible oxide-based thermoelectric materials.

Received 4th May 2022
Accepted 4th July 2022

DOI: 10.1039/d2na00278g

rsc.li/nanoscale-advances

1. Introduction

The rapid development of autonomous, portable and wearable devices and sensors has sparked a great deal of interest in self-sustaining energy sources to replace batteries that are typically limited by shape constraints, periodic recharging and replacement.[1,2] Harvesting electricity from heat using devices made from mechanically flexible thermoelectric materials is promising for such applications.[3–6] Besides a high thermoelectric figure of merit $ZT = \alpha^2\sigma T/\kappa$ (α is the Seebeck coefficient, σ and κ the electrical and thermal conductivities, respectively, and T the absolute temperature[7–9]) for efficient energy conversion, properties such as high mechanical flexibility and toughness are key requirements.

Conducting polymer-based organic thermoelectric materials are mechanically flexible and exhibit ZT values as high as 0.42,[10–17] but are unsuitable for higher than near-room-temperature applications. Purely inorganic thermoelectrics[18] are usually brittle. Integrating nanograined films or nanocrystal assemblies of inorganic thermoelectrics, *e.g.*, $Bi_{2-x}Sb_xTe_3$, on flexible substrates that can withstand moderately high temperatures addresses these challenges to some extent, and yield $\alpha^2\sigma$ values up to 0.2 mW m^{-1} K^{-2} at ~200 °C.[19,20] Semiconductors with extraordinary metal-like ductility, *e.g.*, Ag_2S, and Ag_2Se also hold promise as free-standing thermoelectric materials that obviate flexible substrates.[21–23]

Oxide-based thermoelectric films on layered substrates such as mica offer greater stability at even higher temperatures and can become viable alternatives if high α and σ, are achieved together with high mechanical flexibility.[24,25] Calcium cobaltate $Ca_3Co_4O_9$ is an attractive p-type thermoelectric that exhibits inherently high α and high σ due to its layered crystal structure.[26–30] The thermoelectric properties of layered cobaltates can be improved by nanostructuring, such as fabricating a high-quality single-phase,[31,32] nanostructuring approaches,[33] elemental doping,[34] growing textured films with *c*-axis orientation.[35] However, the thermal conductivity was normally increased with the improving electrical conductivity.[36,37] Introducing nanoscale with dimensions mainly in the ranges of phonon mean free paths is a possible approach to reduce thermal conductivity without inhibiting electrical conductivity due to phonon mean free paths are typically significantly higher than electronic mean free paths. The textured nanograins and faceted nanopores not only offer additional means to lower the κ,[38,39] but also alleviate the brittleness.[40,41] Flexible porous nanograined $Ca_3Co_4O_9$ films obtained by annealing CaO/CoO reactant multilayers exhibit power factors as high a 0.23 mW

[a]*Thin Film Physics Division, Department of Physics, Chemistry and Biology (IFM), Linköping University, SE-58183 Linköping, Sweden. E-mail: binbin.xin@liu.se; per.eklund@liu.se*

[b]*Department of Materials Science and Engineering, Rensselaer Polytechnic Institute, Troy, New York 12180, USA*

[c]*Rensselaer Polytechnic Institute, Department of Mechanical, Aerospace, and Nuclear Engineering, Troy, NY 12180, USA*

† Electronic supplementary information (ESI) available. See https://doi.org/10.1039/d2na00278g

m^{-1} K^{-2} at room temperature.[40] To further increase the porosity of nanoporous $Ca_3Co_4O_9$ films retaining α and σ, it might be an effective way to further reduce κ and improve flexibility.

Here, we demonstrate that nanoporosity characteristics in $Ca_3Co_4O_9$ films can be controlled by adjusting the reactant bilayer thickness in multilayer stacks. The porosities change from 11.2 to 17.1%. The nanoporous films show high σ with a narrow range from 80 to 95 S cm^{-1} and high α of ~130 to ~135 μV K^{-1}, which are close to the values.[42–44] The film with the highest porosity 17.1% has the lowest κ (~0.87 W m^{-1} K^{-1}). The nanoporous $Ca_3Co_4O_9$ films exhibit greater mechanical compliance and resilience to bending than the bulk. Our findings showing pore engineering of layered-ceramics is attractive for realizing mechanically flexible thermoelectrics.

2. Experimental section

Nanoporous $Ca_3Co_4O_9$ thin films were synthesized by annealing $Ca(OH)_2/Co_3O_4$ multilayers on muscovite mica(00*l*) substrates. CaO/Co_3O_4 multilayers were deposited at 600 °C by reactive RF-magnetron sputtering from Ca and Co targets with a 2 mTorr plasma of a 0.5% O_2/99.5% Ar gas mixture[40]. Ambient air-exposure of the CaO/Co_3O_4 multilayers for one month resulted in $Ca(OH)_2/Co_3O_4$ multilayers *via* CaO hydration into $Ca(OH)_2$.[45] Subsequent annealing $Ca(OH)_2/Co_3O_4$ multilayers at 700 °C for 2 hours in air led to nanoporous $Ca_3Co_4O_9$ formation. We prepared five sets of multilayers with different $Ca(OH)_2/Co_3O_4$ bilayer thicknesses, b_t. The deposition times for CaO and Co_3O_4 were varied while keeping the total nominal multilayer thickness constant at ~140 nm. The individual thicknesses of $Ca(OH)_2$ and Co_3O_4 layers in each multilayer film were identical, *i.e.*, $b_t/2$. Thus, altering the bilayer thickness in the $12 \leq b_t \leq 50$ nm range is equivalent to varying the number of bilayers b_n in the $21 \geq b_n \geq 5$ range.

Phase identification was carried out by X-ray diffractometry (XRD) using a PANalytical X'Pert PRO instrument with monochromatic Cu Kα radiation ($\lambda = 1.5406$ Å) and a Ni filter. X-ray reflectivity (XRR) measurements were carried out in a PANalytical Empyrean diffractometer equipped with a copper Cu Kα source with a hybrid mirror on the incidence beam path, a triple-axis Ge 220 analyzer on the diffracted beam path, and a PIXcel3D detector operated in open detection mode. The XRR data were fitted using the X'Pert reflectivity program.

Scanning electron microscopy (SEM) and energy dispersive X-ray (EDX) spectroscopy were carried out in a LEO Gemini 1550 Zeiss instrument operated at 10 kV to characterize film morphology and composition. The surface porosity fraction was determined by analyses of SEM micrographs using the Java version of image J software[46,47]. Most of the nanopores were hexagonal in shape. The average nanopore sizes were estimated from the nanopore area with an uncertainty of 20%, by assuming all the pores to be regular hexagons. The average nanopore size is equal to $L + 2L \cos 60°$ where L is hexagon side length. Transmission electron microscopy (TEM) was carried out in a FEI Tecnai G2 TF20 UT instrument operated at 200 kV on multilayer cross-sections prepared by face-to-face gluing of two sample pieces and mounting them on a Ti grid. The samples were mechanically polished down to 50 μm and ion-milled in a Gatan system with 2–5 kV Ar^+ beams incident at 5°.

Electrical conductivity σ was determined from the sheet resistance measured with a four-point probe Jandel RM3000 station and the film thickness determined from cross-sectional TEM images. Seebeck coefficient α was determined from the slope of the temperature gradient–voltage characteristics measured in a homemade Seebeck measurement setup system equipped with two K-type thermocouples placed at the same position as two Cu electrodes, a Keithley 2001 multimeter, two Peltier elements acting as temperature controller, and two thermometers[45,48].

Thermal conductivity of the annealed $Ca_3Co_4O_9$ film-on-mica samples was determined by non-contact scanning thermal microscopy (SThM) described elsewhere[49–52]. This technique utilizes a Joule-heated 5 μm-diameter Wollaston wire probe, whose thermal resistance was measured in air at 100 nm above the sample surface based on temperature-induced changes in the electrical resistance of the probe and the dissipated Joule heating power. For each film, we measured thermal resistance at three different locations on the sample surface. Thermal conductivity was determined by fitting the thermal resistance data with a 3D finite element model (3DFEM) of the probe-to-sample surface heat transfer assuming isotropic thermal properties for the films and the substrate.

Mechanical flexibility was evaluated by estimating the elastic moduli of the films by surface Brillouin scattering (SBS) spectroscopy and measuring bending-induced relative changes in electrical resistance. SBS spectra were collected by using a JSR Scientific Instruments six-pass high-contrast Fabry–Perot interferometer equipped with a 532.18 nm Verdi V2 DPSS green laser probe. Surface Rayleigh and Sezawa wave velocities were obtained by using $V = (\lambda_0 \Delta f)/(2 \sin \theta_s)$, where λ_0 is the laser wavelength, Δf the Brillouin frequency shift, and θ_s the scattering angle.[53] For the bending tests, we measured the normalized electrical resistance change $\Delta R/R_0$ for different bending radii and cycles, where the initial resistance R_0 includes contact resistances. A constant resistance during bending corresponds to $\Delta R/R_0 = 0$ and indicates good mechanical flexibility and retention of electrical properties.

3. Results and discussion

X-ray diffractograms acquired immediately after deposition for all b_t values investigated show 111 and 222 Bragg reflections from CaO besides those from the mica substrate (Fig. 1a). The 400 diffraction peaks reflected from Co_3O_4 is overwhelmed by a stronger 00*l* reflection from the mica substrate (Fig. 1a) but is observable in diffractograms from as-deposited films on sapphire (Fig. 1b). Films on sapphire also show a weak 111 peak from CoO. The CaO and Co_3O_4 peaks intensities, normalized to that of the 004 mica substrate reflection and sapphire reflection, increase with increasing b_t (Fig. 1c).

Air-exposure of the as-deposited multilayers growing on mica and sapphire leads to the diminution and eventual disappearance of the CaO 111 and 222 peaks (see Fig. 2a and b). Multilayers on sapphire also show a similar behaviour besides

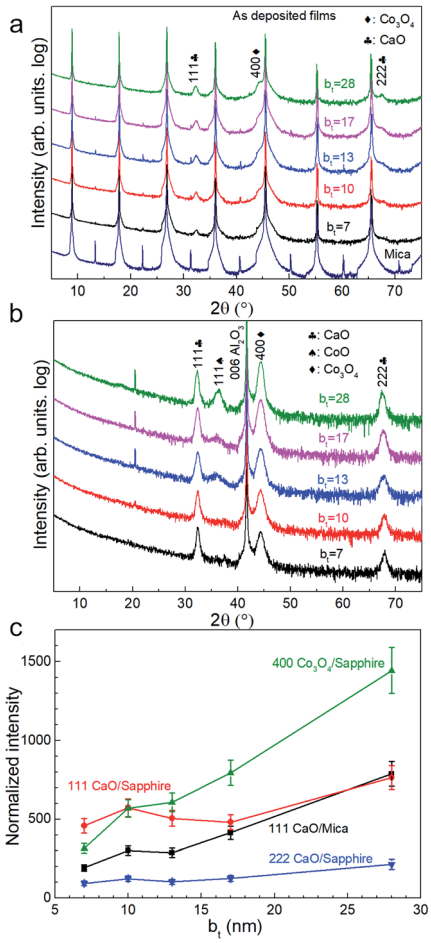

Fig. 1 X-ray diffractograms from as-deposited CaO/Co_3O_4 multilayers with different bilayer thicknesses b_t, on (a) mica (00*l*), and (b) sapphire (006) substrates. (c) CaO and Co_3O_4 peak intensities normalized with the intensity of the corresponding substrate peak, plotted as a function of b_t.

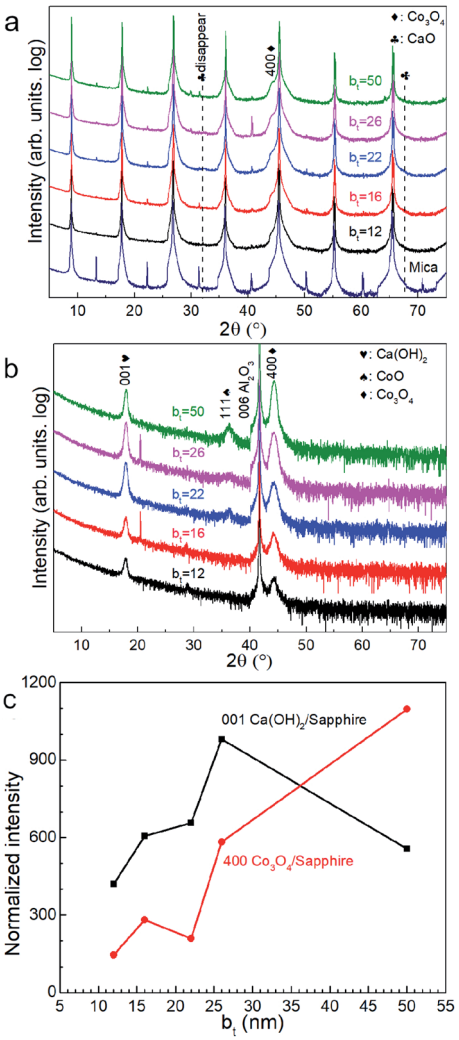

Fig. 2 X-ray diffractograms from $Ca(OH)_2/Co_3O_4$ multilayers formed by air-exposure of CaO/Co_3O_4 multilayers with different bilayer thicknesses between $12 \leq b_t \leq 50$ nm on (a) mica (00*l*) and (b) sapphire (006) substrates. (c) $Ca(OH)_2$ and Co_3O_4 peak intensities normalized to that of the 006 peak from the sapphire substrate, plotted as a function of b_t.

revealing a concomitant emergence of the $Ca(OH)_2$ 001 peak. This peak is not observable in diffractograms from films on mica due to substrate peak overlap. These results are indicative of the conversion of CaO to $Ca(OH)_2$ through ambient moisture uptake.[45] We note that the intensities of the $Ca(OH)_2$ and Co_3O_4 peaks increase with increasing b_t, the intensity of $Ca(OH)_2$ is not the highest when the b_t is 50 nm (Fig. 2c).

Air-exposed CaO/Co_3O_4 multilayers specified by low b_t (*e.g.*, ~12 nm) consist of equiaxed grains of $Ca(OH)_2$ and Co_3O_4 without any discernible interfaces (Fig. 3a). EDX spectral maps of Ca and Co indicate that $Ca(OH)_2$ and Co_3O_4 are interspersed across individual layers (Fig. 3a inset). This result is consistent with Co_3O_4 layers comprised of discontinuous grains that facilitate moisture intake and transport, as suggested in our recent work.[45] Air-exposed multilayers with $b_t = 16$ nm exhibit more distinct $Ca(OH)_2/Co_3O_4$ interfaces (Fig. 3b). The Ca-containing layers that appear brighter due to a higher Z-contrast are about 81% thicker than the Co_3O_4 layers, consistent with a 95.2% unit cell volume expansion caused by the CaO → $Ca(OH)_2$ conversion during air-exposure. For $b_t > 16$ nm, TEM images show distinct Co- and Ca-containing layers, but with a greater interface roughness that increases with b_t. Such interface roughening is attributable to the higher volume $Ca(OH)_2$ grains encroaching into the nearly unchanged adjacent Co_3O_4 layers. For $b_t = 50$ nm, the thickness of $Ca(OH)_2$ layer in top larger than that in bottle near mica, which may be due to the low hydration reactions by preventing of thicker Co_3O_4 layers and lead to the low intensity of $Ca(OH)_2$ 001 in Fig. 2c. SAED patterns indicate increased in-plane grain texturing with increasing b_t (see Fig. 3c and d). EDX spectral maps from air-exposed films with higher b_t show distinct Co-containing layers, in contrast to the uniform distribution of Ca, indicating Ca diffusion (see ESI Fig. S1†). Our results indicate that the bilayer thickness needs to be greater than a critical value of b_t > 12 nm to form layers structure with sharp interfaces.

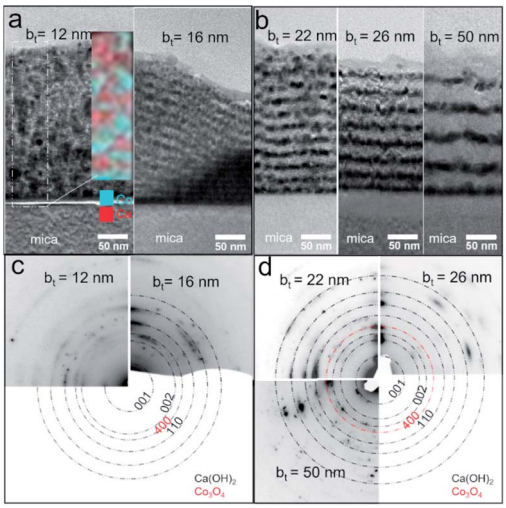

Fig. 3 (a and b) Cross-sectional bright-field TEM images and (c and d) selected-area electron diffraction (SAED) patterns from $Ca(OH)_2/Co_3O_4$ multilayers with different bilayer thicknesses b_t.

Otherwise, EDS maps from multilayers with $b_t = 16$ nm show clear Co layers and almost uniform distribution Ca elements in multilayers (see ESI Fig. S1a†).

X-ray diffractograms show that annealing the $Ca(OH)_2/Co_3O_4$ multilayers leads to $Ca_3Co_4O_9$ formation through a reaction between the Co_3O_4 and $Ca(OH)_2$ layers (Fig. 4a). The exclusive presence of multiple 00*l* peak reflections of $Ca_3Co_4O_9$ indicate textured basal planes oriented parallel to the substrate surface. The $Ca_3Co_4O_9$ grain size is largest for films specified by $b_t = 22$ nm, as indicated by the narrowest width of the $Ca_3Co_4O_9$ 002 reflection.

Surfaces of the annealed films exhibit faceted intergranular nanopores (see Fig. 5). Films with the smallest b_t in our studies reveal a relatively rough surface, probably due to the edge-on orientation of some platelet-shaped grains on the surface (see Fig. 5a). In contrast, annealed films with $b_t \geq 16$ nm exhibit smoother surfaces, with faceted nanopores between hexagonal terraces and plate-shaped grains (Fig. 5b–e). The average pore size increases monotonically from around 120 to 400 nm with increasing b_t from 12 nm to 50 nm (see Fig. 5f). The porosity fraction increases with b_t from 3.7% to 17.1% for $12 \leq b_t \leq 26$ nm but drops to 13.4% for $b_t = 50$ nm (Fig. 5f).

Cross-sectional TEM micrographs of films obtained by annealing $Ca(OH)_2/Co_3O_4$ multilayers with $12 \leq b_t \leq 50$ nm created from CaO/Co_3O_4 multilayers (Fig. 6a–e) reveal a polycrystalline $Ca_3Co_4O_9$ layer separated from the substrate by an amorphous glass layer.[40] Lattice images for the $Ca_3Co_4O_9$ layer and SAED patterns (Fig. 6f–j) confirm that the (001) basal planes are oriented parallel to the film surface, corroborating our XRD and SEM results. The in-plane/out-of-plane aspect ratio of the pores is about four for the film with $b_t = 50$ nm (Fig. 6e). This observation is consistent with the SEM results and our recent work[45] indicating that oriented nanopore formation arises from basal plane removal driven by local densification of textured $Ca_3Co_4O_9$. For all b_t values except $b_t = 50$ nm, we observe nanopores spanning across the $Ca_3Co_4O_9$ layers and microporous gaps at the $Ca_3Co_4O_9$ – amorphous layer interface and interlayer nanoporosity (see Fig. 6a–e). No microporous gaps or interlayer porosity are discernible in the amorphous layers.

TEM micrographs reveal that for all our films, the $Ca_3Co_4O_9$ layer thickness is around twice the amorphous layer thickness (Fig. 7). Increasing the b_t from 12 nm to 26 nm increased the $Ca_3Co_4O_9$ layer thickness from 170 ± 10 nm to 193 ± 10 nm but decreased the amorphous layer thickness from 103 nm to 73 nm. EDX analyses of the amorphous layer revealed O, Al, Si and Ca (ESI Fig. S2†), but no traces of Co above the EDX detection limit. These results suggest that the amorphous layer is formed due to preferential Ca diffusion and incorporation into the mica substrate. This inference is supported by the inverse correlation between amorphous layer thickness and b_t and the higher Ca/Co ratio of 55 : 45 in multilayer than that in the $Ca_3Co_4O_9$ layer. The anomalously low $Ca_3Co_4O_9$ layer thickness of 159 ± 10 nm for $b_t = 50$ nm is likely an outlier due to a very low surface porosity fraction of 13.4% and no microporous gaps at the $Ca_3Co_4O_9$ – amorphous layer interface and needs further study.

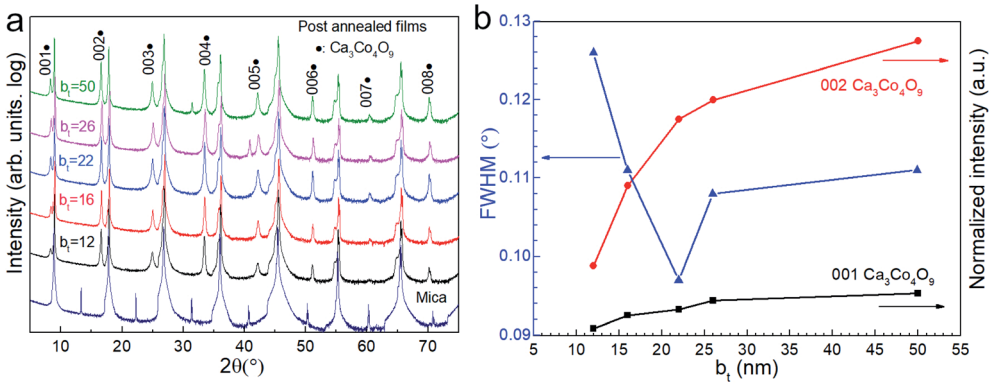

Fig. 4 (a) X-ray diffractograms showing $Ca_3Co_4O_9$ formation on mica (00*l*) substrate by annealing $Ca(OH)_2/Co_3O_4$ multilayers with different bilayer thicknesses in the $12 \leq b_t \leq 50$ nm range. (b) $Ca_3Co_4O_9$ 001 and 002 peak intensities normalized with the intensity of the corresponding substrate peaks, plotted as a function of b_t.

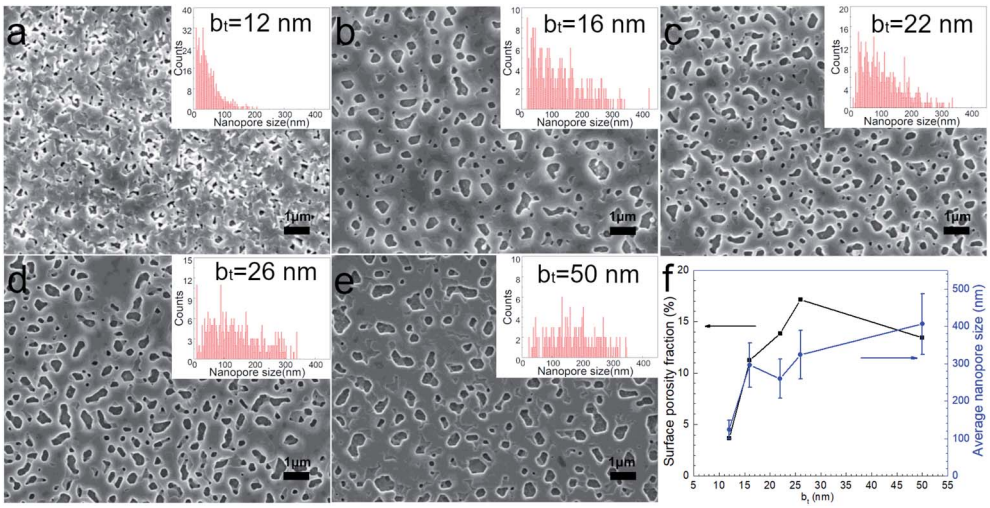

Fig. 5 (a–e) SEM images from annealed $Ca(OH)_2/Co_3O_4$ multilayers with $12 \leq b_t \leq 50$ nm grown on mica (00l) substrates. (f) Surface porosity fraction determined from SEM image analyses.

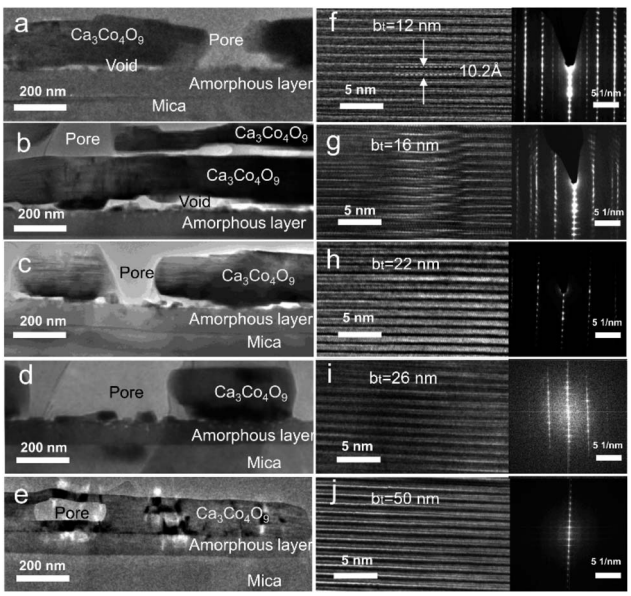

Fig. 6 (a–e) Cross-sectional bright-field TEM images from $Ca_3Co_4O_9$ films obtained by annealing $Ca(OH)_2/Co_3O_4$ multilayers with $12 \leq b_t \leq 50$ nm created from CaO/Co_3O_4 multilayers. (f–j) The corresponding high-resolution TEM images and SAED patterns capturing the layered atomic structure of $Ca_3Co_4O_9$.

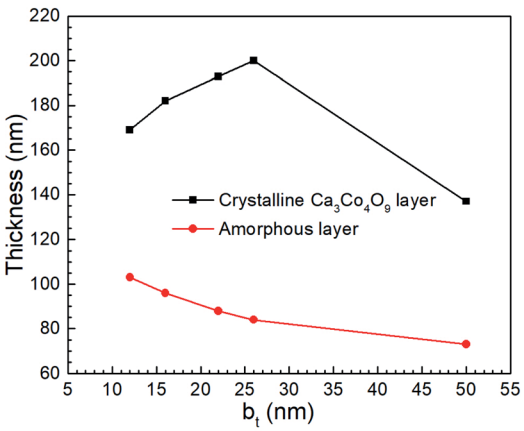

Fig. 7 The thicknesses of crystalline $Ca_3Co_4O_9$ and amorphous layers in porous films obtained by annealing $Ca(OH)_2/Co_3O_4$ multilayers created from CaO/Co_3O_4 multilayers with $12 \leq b_t \leq 50$ nm.

Thermoelectric properties

Considering that amorphous materials normally have lower electrical conductivity σ than corresponding crystalline materials and the amorphous layer has a low thermal conductivity κ, the amorphous oxide layer is assumed as an insulator. The electrical conductivity σ of $Ca_3Co_4O_9$ films slightly increases with b_t (Fig. 8a) and peaks around 13% porosity (Fig. 8b). For example, $\sigma \sim 90$ S cm^{-1} for the film with higher porosity (13.8%) is 50% higher than for the film with lowest porosity (3.7%). But σ for the film with different porosities from 11.2 to 17.1% shows a narrow range from 80 to 95 S cm^{-1}. The reason may be that the rough morphology and lowest quality layered structure of annealed film with $b_t = 12$ nm cause lower carrier mobility and the high-quality layered structure of the annealed films with $b_t \geq 16$ nm led to high carrier mobility as shown in Fig. 4 and the size range of nanopores mainly from 120 nm to 400 nm has a slight effect for the electrical conductivity.

The Seebeck coefficient α increases sightly with nanoporosity fraction, *e.g.*, from $\alpha = 128$ μV K^{-1} observed for porosity = 3.7% to $\alpha = 136$ μV K^{-1} for porosity = 17.1%. The power factor increases from 0.96 to 1.53 μW cm^{-1} K^{-2} with increasing porosity (Fig. 8b). The highest power factor is $\alpha^2\sigma = 1.63$ μW cm^{-1} K^{-2} for the film with $b_t = 50$ nm with highest σ.

We used 3DFEM model fitting[49] to determine the effective thermal conductivity κ_{film} of the $Ca_3Co_4O_9$ films (see Fig. 9) by using a mica substrate thermal conductivity value of $\kappa_{sub} = 0.421$ W m^{-1} K^{-1}, determined by SThM probe measurements.

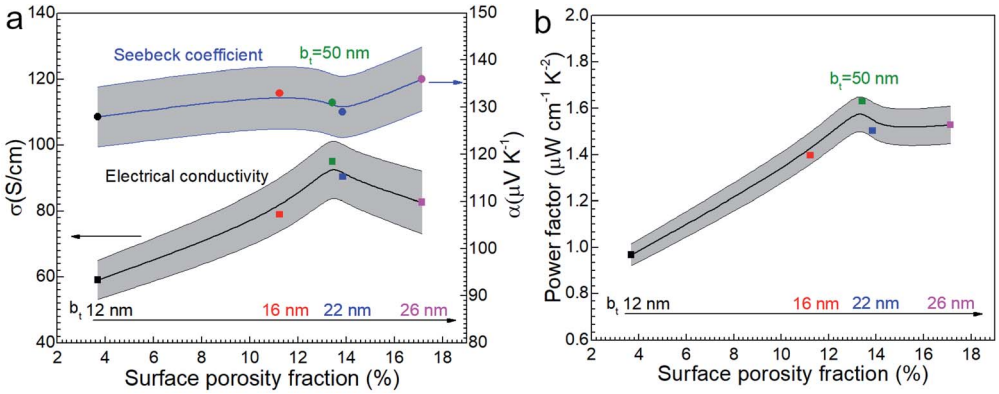

Fig. 8 (a) The electrical conductivity σ and the Seebeck coefficient α and (b) power factor $\alpha^2\sigma$ of nanoporous $Ca_3Co_4O_9$ films as function of surface porosity fraction at room temperature.

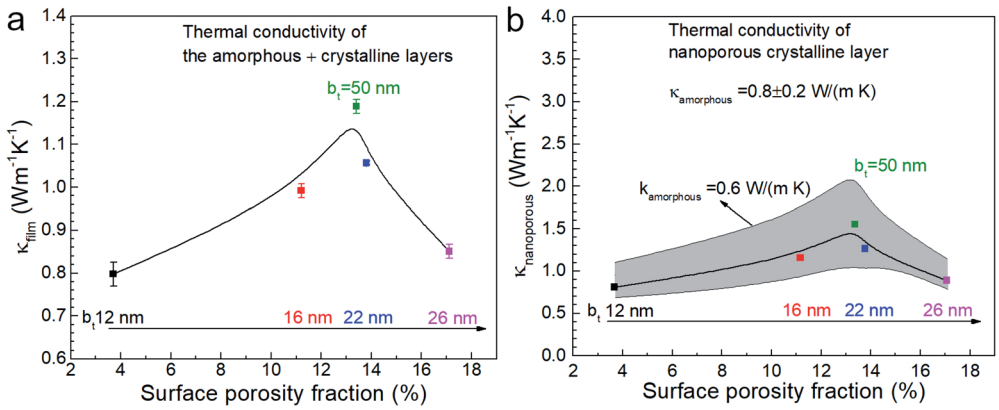

Fig. 9 (a) Effective thermal conductivity κ film of $Ca_3Co_4O_9$ films as a function of surface porosity fraction, and (b) thermal conductivity of the nanoporous crystalline $Ca_3Co_4O_9$ layer $\kappa_{nanoporous}$, assuming $\kappa_{amorphous} = 0.8$ W m^{-1} K^{-1} with a ± 0.2 W m^{-1} K^{-1} uncertainty captured by error bars.

Since κ_{film} depends on the thermal conductivities of the amorphous ($\kappa_{amorphous}$) and nanoporous crystalline ($\kappa_{nanoporous}$) layers, both of which are unknown, we computed $\kappa_{nanoporous}$ by using a one-dimensional cross-plane thermal resistance network model for the crystalline-amorphous bilayer described by $\frac{t_{nanoporous}}{\kappa_{nanoporous}} = \frac{t_{total}}{\kappa_{film}} - \frac{t_{amorphous}}{\kappa_{amorphous}}$. We selected three possible $\kappa_{amorphous}$ values of 0.6, 0.8, and 1 (0.8 ± 0.2) W m^{-1} K^{-1}, which are comparable to the thermal conductivity of amorphous silica.[54] We assumed $\kappa_{amorphous}$ to be identical in all the five samples with $50 \geq b_t \geq 12$ nm and used the measured amorphous layer thickness for each sample, *i.e.*, 73 nm $\leq t_{amorphous} \leq$ 103 nm. This model is apt because both the amorphous and the nanoporous regions are much thinner than the ~5 μm probe-sample heat transfer radius and have low values of fitted thermal conductivities.

Plotting the effective κ_{film} and the values extracted for $\kappa_{nanoporous}$ of the nanoporous layer as a function of porosity (see Fig. 9a and b) reveal peaks in both κ_{film} and $\kappa_{nanoporous}$ around 13% porosity, at which σ also peaks, as shown earlier. We note that decreasing assumed $\kappa_{amorphous}$ yields a higher $\kappa_{nanoporous}$. Both the κ_{film} and σ are low for the lowest porosity film due to the relatively higher surface roughness compared to the other films. The film with the highest porosity 17.1% (*i.e.*, with $b_t = 26$ nm) has the lowest κ (~0.87 W m^{-1} K^{-1}) in annealed films with $b_t \geq 16$ nm. The annealed film with $b_t = 12$ nm shows low κ (~0.8 W m^{-1} K^{-1}) due to the rough morphology.

Mechanical flexibility

Surface Brillouin scattering (SBS) spectra from $Ca_3Co_4O_9$ films (Fig. 10a) reveal stiffness values that are significantly lower than that of bulk $Ca_3Co_4O_9$. Rayleigh peaks are seen around ± 8.5 GHz at scattering angles $\theta_s \geq 70°$. At lower scattering angles, the Rayleigh peaks merge into the central elastic peak, and we observe Sezawa peaks around ±11.5 GHz. Sezawa peaks are typical of soft films on hard substrates,[55] as is our case for $Ca_3Co_4O_9$ on sapphire. The invariance of the surface Rayleigh velocity with $k\|d$ (Fig. 10b) within experimental uncertainties is indicative of the elastic properties of the $Ca_3Co_4O_9$ film with negligible influence of the sapphire substrate. In contrast, the Sezawa velocity increases substantially with decreasing $k\|d$ due to the hard sapphire substrate. We calculated the shear modulus G of the nanoporous $Ca_3Co_4O_9$ film from

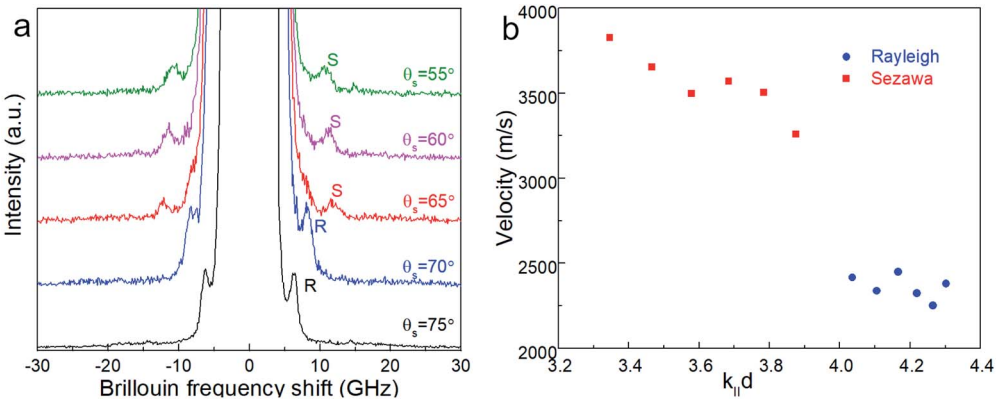

Fig. 10 (a) Representative Brillouin spectra from a ~185 nm-thick nanoporous $Ca_3Co_4O_9$ film (corresponding to $b_t = 26$ nm) on sapphire for different scattering angles θ_s showing Rayleigh (R) and Sezawa (S) peaks. (b) Surface Rayleigh and Sezawa velocities plotted a of $k\|d$, where $k\| = (4\pi \sin \theta_s)/\lambda_0$ is the surface acoustic wave vector, and d the film thickness.

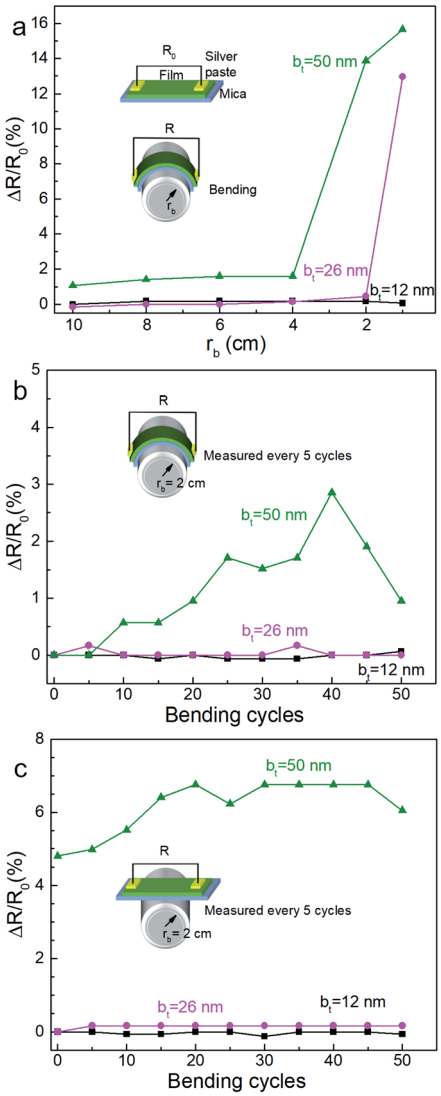

Fig. 11 The normalized resistance changing $\Delta R/R_0$ of the $Ca_3Co_4O_9$ films on mica (00l) substrates obtained by reactions of multiple stacks of $Ca(OH)_2/Co_3O_4$ bilayers with $12 \leq b_t \leq 50$ nm as a function of (a) bending radius r_b and (b) the number of bending cycles at a bending radius of 2 cm, and (c) after restoration to non-bent geometry.

$V_{\text{Rayleigh}} = \beta\sqrt{\frac{G}{\rho}}$, where ρ is the density and $\beta = 0.94$.[56,57] Assuming isotropy, invoking $E = 2G(1 + \nu)$, using the bulk $Ca_3Co_4O_9$ Poisson's ratio $\nu = 0.31$,[58] and a density $\rho \sim 3.0$ g cm^{-3} for the nanoporous $Ca_3Co_4O_9$ film determined from X-ray reflectivity measurements (ESI Fig. S3†), we get Young's and shear moduli values of $G = 18.92 \pm 1.14$ GP, and $E = 49.62 \pm 2.99$ GPa, respectively. Both these values for nanoporous $Ca_3Co_4O_9$ film are 52.7% lower than the predicted values of $G = 39.98$ GPa and $E = 104.86$ for bulk $Ca_3Co_4O_9$.[58] The 21% lower density of the nanoporous $Ca_3Co_4O_9$ film compared to bulk $Ca_3Co_4O_9$ (3.8 g cm^{-3}) partially explains the lower moduli. We propose that the low atomic bond density near the nanopore walls in the film also contribute to the increased mechanical compliance.

Mechanical bending of the film-substrate composite showed a high retention of the electrical properties, consistent with high mechanical compliance indicated by the SBS results. Two-point resistance of the film measured as a function of bending radius r_b (see Fig. 11a) showed negligible changes in the normalized resistance ($\Delta R/R_0 \sim 0$) for $r_b \geq 4$ cm, where R_0 is the initial resistance for each film, indicating good mechanical flexibility and low electromechanical coupling. Films synthesized from multilayers specified by $b_t = 12$ nm and $b_t = 26$ nm show a greater resilience to bending and bend cycling than the film corresponding to $b_t = 50$ nm (Fig. 11b and c). While further studies are needed to understand correlations between nanoporosity, bend cycling, and mechanical compliance, our results clearly indicate that the nanoporous films are mechanically flexible and have a low electromechanical coupling for a large range of b_t and bending.

Conclusions

We have synthesized $Ca_3Co_4O_9$ films with different porosities by annealing multilayers of calcium and cobalt oxide bilayers specified by $Ca(OH)_2/Co_3O_4$ bilayer thicknesses b_t. Increasing b_t increases the nanoporosity fraction and average nanopore size in the $Ca_3Co_4O_9$ film formed during annealing. The higher

porosity films exhibit a 50% higher electrical conductivity as well as a high Seebeck coefficient, together with a low thermal conductivity. The nanoporous $Ca_3Co_4O_9$ films show a higher mechanical compliance than the bulk $Ca_3Co_4O_9$ and are resilient to mechanical bending and bend cycling. These results indicate that engineering nanoporosity in layered oxides through reactions of multilayer stacks of component oxides could be attractive for achieving mechanically-flexible high-figure-of-merit thermoelectric nanomaterials for emergent applications.

Author contributions

Binbin Xin: performed experiments, data collection and analysis, writing – original draft, and writing – review & editing; Erik Ekström: magnetron sputtering; Jun Lu and Anna Elsukova: TEM data; Yueh-Ting Shih and Liping Huang: surface Brillouin scattering (SBS) spectroscopy; Yun Zhang, Wenkai Zhu, and Theodorian Borca-Tasciuc: thermal conductivity; Biplab Paul and Per Eklund: experiment design and supervision; Erik Ekström, Yueh-Ting Shih, Liping Huang, Jun Lu, Anna Elsukova, Yun Zhang, Wenkai Zhu, Theodorian Borca-Tasciuc, Ganpati Ramanath, Arnaud Le Febvrier, Biplab Paul and Per Eklund: writing – review & editing.

Conflicts of interest

The authors declare no conflicts of interest.

Acknowledgements

The authors acknowledge support from the Knut and Alice Wallenberg Foundation through the Wallenberg Academy Fellows program (grant no. KAW 2020.0196), the Swedish Research Council under project grant no 2021-03826, the Swedish Government Strategic Research Area in Materials Science on Functional Materials at Linköping University (Faculty Grant SFO-Mat-LiU No. 2009 00971), and the Swedish Energy Agency under project 46519-1. B. X. also acknowledges financial support from the China Scholarship Council. GR acknowledges funding from the grant CMMI 2135725 from the National Science Foundation.

References

1 N.-S. Choi, Z. Chen, S. A. Freunberger, X. Ji, Y. Sun, K. Amine, G. Yushin, L. F. Nazar, J. Cho and P. G. Bruce, *Angew. Chem., Int. Ed.*, 2012, **51**, 9994–10024.
2 E. Vinodkumar, M. Rotem, E. Ran, S. Gregory and A. Doron, *Energy Environ. Sci.*, 2011, **4**, 3243–3262.
3 R. Tian, C. Wan, N. Hayashi, T. Aoai and K. Koumoto, *MRS Bull.*, 2018, **43**, 193–198.
4 C. S. Kim, H. M. Yang, J. Lee, G. S. Lee, H. Choi, Y. J. Kim, S. H. Lim, S. H. Cho and B. J. Cho, *ACS Energy Lett.*, 2018, **3**, 501–507.
5 Y. Du, J. Xu, B. Paul and P. Eklund, *Appl. Mater. Today*, 2018, **12**, 366–388.
6 B. J. Hyeong, F. Haiyu, Y. Kazuaki and S. Ali, *J. Mater. Chem. C*, 2015, **3**, 10362–10374.
7 F. J. DiSalvo, *Science*, 1999, **285**, 703–706.
8 J. He and T. M. Tritt, *Science*, 2017, **357**, eaak9997.
9 A. M. Dehkordi, M. Zebarjadi, J. He and T. M. Tritt, *Mater. Sci. Eng., R*, 2015, **97**, 1–22.
10 D. Ni, H. Song, Y. Chen and K. Cai, *Energy*, 2019, **170**, 53–61.
11 O. Bubnova, Z. U. Khan, A. Malti, S. Braun, M. Fahlman, M. Berggren and X. Crispin, *Nat. Mater.*, 2011, **10**, 429–433.
12 B. Olga and C. Xavier, *Energy Environ. Sci.*, 2012, **5**, 9345–9362.
13 Z. Fan, D. Du, Z. Yu, P. Li, Y. Xia and J. Ouyang, *ACS Appl. Mater. Interfaces*, 2016, **8**, 23204–23211.
14 S. Rudd, P. J. Murphy and D. R. Evans, *Synth. Met.*, 2018, **242**, 61–66.
15 H. Song, Q. Meng, Y. Lu and K. Cai, *Adv. Electron. Mater.*, 2019, **5**, 1800822.
16 Y. Akihito and T. Naoki, *J. Electron. Mater.*, 2016, **45**, 2914–2919.
17 Y. Du, H. Li, X. Jia, Y. Dou, J. Xu and P. Eklund, *Energies*, 2018, **11**, 2849.
18 H. Mamur, M. R. A. Bhuiyan, F. Korkmaz and M. Nil, *Renewable Sustainable Energy Rev.*, 2018, **82**, 4159–4169.
19 Q. Jin, S. Jiang, Y. Zhao, D. Wang, J. Qiu, D. M. Tang, J. Tan, D. M. Sun, P. X. Hou, X. Q. Chen, K. Tai, N. Gao, C. Liu, H. M. Cheng and X. Jiang, *Nat. Mater.*, 2019, **18**, 62–68.
20 L.-X. Liang, Y. Deng, Y. Wang, H.-L. Gao and J. Cui, *J. Nanopart. Res.*, 2014, **16**, 1–7.
21 X. Shi, H. Chen, F. Hao, R. Liu, T. Wang, P. Qiu, U. Burkhardt, Y. Grin and L. Chen, *Nat. Mater.*, 2018, **17**, 421–426.
22 J. Liang, T. Wang, P. Qiu, S. Yang, C. Ming, H. Chen, Q. Song, K. Zhao, T.-R. Wei, D. Ren, Y.-Y. Sun, X. Shi, J. He and L. Chen, *Energy Environ. Sci.*, 2019, **12**, 2983–2990.
23 H. Wang, X. Liu, Z. Zhou, H. Wu, Y. Chen, B. Zhang, G. Wang, X. Zhou and G. Han, *Acta Mater.*, 2022, 223.
24 R. Jayakanth, *J. Mater. Res.*, 2016, **32**, 183–203.
25 B. Paul, V. Khranovskyy, R. Yakimova and P. Eklund, *Mater. Res. Lett.*, 2019, **7**, 239–243.
26 D. Kenfaui, M. Gomina, J. G. Noudem and D. Chateigner, *Materials*, 2018, **11**, 1224.
27 P. Brinks, N. Van Nong, N. Pryds, G. Rijnders and M. Huijben, *Appl. Phys. Lett.*, 2015, **106**, 143903.
28 S. Bresch, B. Mieller, C. Selleng, T. Stöcker, R. Moos and T. Rabe, *J. Electroceram.*, 2018, **40**, 225–234.
29 P. Wannasut, N. Keawprak, P. Jaiban and A. Watcharapasorn, *IOP Conf. Ser.: Mater. Sci. Eng.*, 2018, **303**, 012010.
30 B. Paul, J. L. Schroeder, S. Kerdsongpanya, N. V. Nong, N. Schell, D. Ostach, J. Lu, J. Birch and P. Eklund, *Adv. Electron. Mater.*, 2015, **1**, 1400022.
31 M.-G. Kang, K.-H. Cho, J.-S. Kim, S. Nahm, S.-J. Yoon and C.-Y. Kang, *Acta Mater.*, 2014, **73**, 251–258.
32 M. Shikano and R. Funahashi, *Appl. Phys. Lett.*, 2003, **82**, 1851–1853.

33 M.-E. Song, H. Lee, M.-G. Kang, W. Li, D. Maurya, B. Poudel, J. Wang, M. A. Meeker, G. A. Khodaparast, S. T. Huxtable and S. Priya, *ACS Omega*, 2018, **3**, 10798–10810.
34 J. Yu and R. Freer, *J. Phys.: Energy*, 2022, **4**, 022001.
35 X. Zhu, D. Shi, S. Dou, Y. Sun, Q. Li, L. Wang, W. Li, W. Yeoh, R. Zheng and Z. Chen, *Acta Mater.*, 2010, **58**, 4281–4291.
36 E. G. Masashi Mikami and R. Funahashi, *J. Mater. Res.*, 2005, **20**, 2491–2497.
37 J. Yu, X. Liu, W. Xiong, B. Wang, M. J. Reece and R. Freer, *J. Alloys Compd.*, 2022, 902.
38 B. Paul, Y. Zhang, W. Zhu, B. Xin, G. Ramanath, T. Borca-Tasciuc and P. Eklund, *Appl. Phys. Lett.*, 2022, **120**, 061904.
39 B. Xu, T. Feng, M. T. Agne, L. Zhou, X. Ruan, G. J. Snyder and Y. Wu, *Angew. Chem., Int. Ed.*, 2017, **56**, 3546–3551.
40 B. Paul, E. M. Björk, A. Kumar, J. Lu and P. Eklund, *ACS Appl. Energy Mater.*, 2018, **1**, 2261–2268.
41 B. Paul, J. Lu and P. Eklund, *ACS Appl. Mater. Interfaces*, 2017, **9**, 25308–25316.
42 Y. Yin and A. Tiwari, *Sci. Rep.*, 2021, **11**, 6324.
43 U. Hira, S. S. Ali, S. Latif, N. Pryds and F. Sher, *ACS Omega*, 2022, **7**, 6579–6590.
44 J. Yu, M. Nelo, X. Liu, S. Shao, B. Wang, S. J. Haigh, H. Jantunen and R. Freer, *J. Eur. Ceram. Soc.*, 2022, **42**, 3920–3928.
45 B. Xin, A. L. Febvrier, R. Shu, A. Elsukova, V. Venkataramani, Y. Shi, G. Ramanath, B. Paul and P. Eklund, *ACS Appl. Nano Mater.*, 2021, **4**, 9904–9911.
46 R. Teotia, S. K. Verma, D. Kalita, A. K. Singh, G. Dahe and J. Bellare, *J. Mater. Sci.*, 2017, **52**, 12513–12523.
47 M. U. H. Joardder, C. Kumar, R. J. Brown and M. A. Karim, *J. Food Eng.*, 2015, **166**, 156–164.
48 B. Xin, A. L. Febvrier, L. Wang, N. Solin, B. Paul and P. Eklund, *Mater. Des.*, 2021, **210**, 110033.
49 Y. Zhang, W. Zhu and T. Borca-Tasciuc, *Nanoscale Adv.*, 2021, **3**, 692–702.
50 Y. Zhang, W. Zhu, L. Han and T. Borca-Tasciuc, *Rev. Sci. Instrum.*, 2020, **91**, 014901.
51 Y. Zhang, W. Zhu, F. Hui, M. Lanza, T. Borca-Tasciuc and M. Muñoz Rojo, *Adv. Funct. Mater.*, 2019, **30**, 1900892.
52 Y. Zhang, W. Zhu and T. Borca-Tasciuc, *Oxf. Open Mater. Sci.*, 2021, **1**, itab011.
53 G. Michael and H. Liping, *J. Phys. D: Appl. Phys.*, 2012, **45**, 275302.
54 D. G. Cahill and R. O. Pohl, *Phys. Rev. B: Condens. Matter Mater. Phys.*, 1987, **35**, 4067–4073.
55 C. Sumanya, J. D. Comins and A. G. Every, *Wave Motion*, 2017, **68**, 78–87.
56 B. D. Ozsdolay, X. Shen, K. Balasubramanian, G. Scannell, L. Huang, M. Yamaguchi and D. Gall, *Surf. Coat. Technol.*, 2017, **325**, 572–578.
57 G. Carlotti, *Appl. Sci.*, 2018, **8**, 124.
58 A. Jain, S. P. Ong, G. Hautier, W. Chen, W. D. Richards, S. Dacek, S. Cholia, D. Gunter, D. Skinner, G. Ceder and K. A. Persson, *APL Mater.*, 2013, **1**, 011002.